REPORT

An expanded class of histidine-accepting viral tRNA-like structures

CONNER J. LANGEBERG,[1] MADELINE E. SHERLOCK,[1] ANDREA MACFADDEN,[1] and JEFFREY S. KIEFT[1,2]

[1]Department of Biochemistry and Molecular Genetics, University of Colorado Denver School of Medicine, Aurora, Colorado 80045, USA
[2]RNA BioScience Initiative, University of Colorado Denver School of Medicine, Aurora, Colorado 80045, USA

ABSTRACT

Structured RNA elements are common in the genomes of RNA viruses, often playing critical roles during viral infection. Some viral RNA elements use forms of tRNA mimicry, but the diverse ways this mimicry can be achieved are poorly understood. Histidine-accepting tRNA-like structures (TLS^{His}) are examples found at the 3′ termini of some positive-sense single-stranded RNA (+ssRNA) viruses where they interact with several host proteins, induce histidylation of the RNA genome, and facilitate processes important for infection, to include genome replication. As only five TLS^{His} examples had been reported, we explored the possible larger phylogenetic distribution and diversity of this TLS class using bioinformatic approaches. We identified many new examples of TLS^{His}, yielding a rigorous consensus sequence and secondary structure model that we validated by chemical probing of representative TLS^{His} RNAs. We confirmed new examples as authentic TLS^{His} by demonstrating their ability to be histidylated in vitro, then used mutational analyses to imply a tertiary interaction that is likely analogous to the D- and T-loop interaction found in canonical tRNAs. These results expand our understanding of how diverse RNA sequences achieve tRNA-like structure and function in the context of viral RNA genomes and lay the groundwork for high-resolution structural studies of tRNA mimicry by histidine-accepting TLSs.

Keywords: viral RNA; tRNA mimicry; bioinformatics; aminoacylation; chemical probing

INTRODUCTION

Viruses are obligate cellular parasites that must subvert and coopt host cellular machinery to proliferate. In single-stranded RNA (ssRNA) viruses, structured regions within the viral genomic RNA can directly manipulate cellular machinery, a ubiquitous part of many viruses' overall infection strategy. Such RNA structures affect pathways and processes as diverse as translation, replication, packaging, viral RNA stability, immune evasion, and others (Pathak et al. 2011; Tuplin 2015; Garcia-Blanco et al. 2016; Hogg 2016; Jaafar and Kieft 2019). RNA structural elements frequently coordinate different processes occurring on the genomic RNA, often using conformational changes (Gamarnik and Andino 1998). Understanding the structural diversity and distribution of different viral RNA elements is essential to define their mechanisms of action and helps us understand roles for RNA in cellular processes by revealing the fundamental rules for RNA structure-driven function. In particular, because ssRNA viruses evolve relatively rapidly, exploring conservation of sequence and structure of an RNA class within different viruses reveals how dissimilar RNA sequences achieve a similar structure and function (Mans et al. 1991; Roth and Breaker 2009; Webb et al. 2009; Perreault et al. 2011; Pisareva et al. 2018; Steckelberg et al. 2018; Jones et al. 2021).

A class of structured RNAs with roles in viral infection are the transfer RNA (tRNA)-like structures (TLSs), found in the 3′ terminal sequences of certain positive-sense single-stranded RNA (+ssRNA) viruses where they mimic the structure of tRNAs to varying degrees (Fig. 1A; Rietveld et al. 1984; Mans et al. 1991; Dreher 2010; Felden et al. 1994a,1996; Hammond 2009). These TLSs were first identified by their ability to be aminoacylated on their 3′ ends by host cell aminoacyl tRNA synthetases (AARSs) (Pinck et al. 1970; Ijberg and Philipson 1972; Kohl and Hall 1974; Salomon et al. 1976; Joshi et al. 1985; Goodwin and Dreher 1998). Furthermore, they interact with host proteins associated with tRNAs, specifically eukaryotic elongation factor 1A (eEF1A) (Joshi et al. 1986; Dreher et al. 1999; Zeenko et al. 2002; Hwang et al. 2013; Li et al. 2013), and the C-adding enzyme (Litvak et al. 1973;

Corresponding author: Jeffrey.Kieft@cuanschutz.edu
Article is online at http://www.rnajournal.org/cgi/doi/10.1261/rna.078550.120.

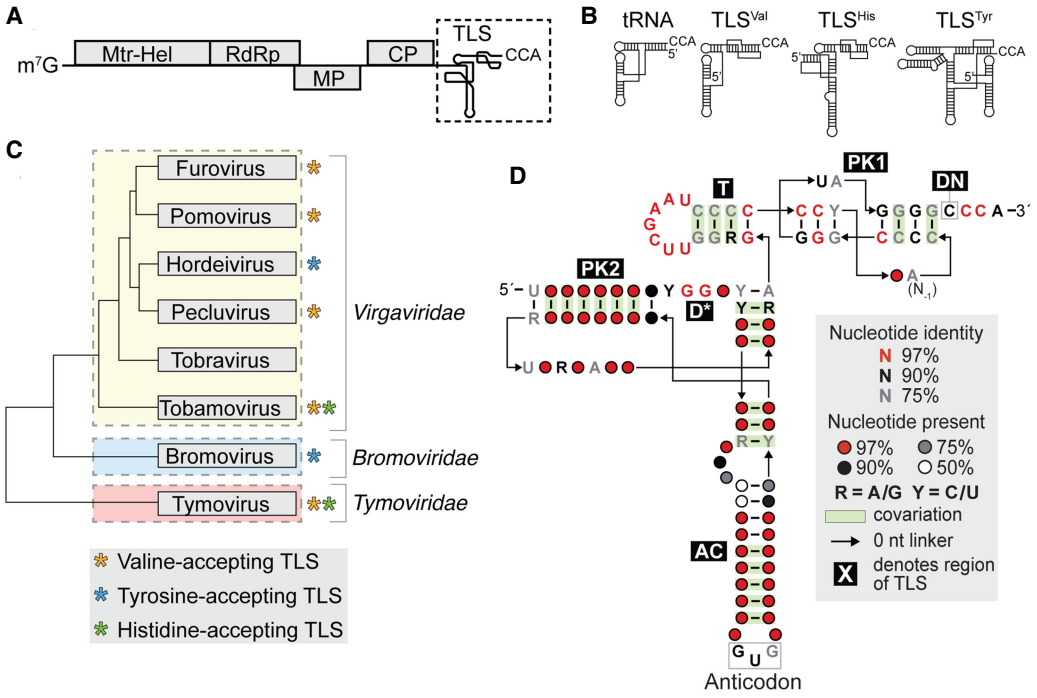

FIGURE 1. Histidine-accepting tRNA-like structures. (*A*) Cartoon diagram of a TLS-containing +ssRNA viral RNA genome, with the 3′ TLS indicated with a dashed box. Gray shaded boxes indicate the ORFs in the capped viral genome. (*B*) Cartoon representations of tRNA and the three classes of TLS. (*C*) Phylogenetic distribution of tRNA-like structures in several +ssRNA plant virus genera. Tree is based on the concatenated viral methyl transferase, replicative RNA helicase, and RNA dependent RNA polymerase (Mtr-Hel-RdRp) sequence, adapted from King et al. (2012). Asterisks denote the presence of one or more tRNA-like structure classes in each viral genus. (*D*) Consensus sequence and secondary structural model of the 157 identified unique histidine-accepting tRNA-like structure sequences. Regions are labeled relative to their homology in a canonical tRNA, if present. PK2: pseudoknot 2 region, D*: putative D-loop analog, AC: anticodon arm, T: T-arm, PK1: pseudoknot 1 region, DN: discriminator nucleotide. The location of an A base speculated to substitute for the N_{-1} G in authentic $tRNA^{His}$ is indicated.

Dreher and Goodwin 1998; Hema et al. 2005). However, although TLS RNAs have a terminal CCA that matches the CCA in tRNA and that is aminoacylated, they have secondary structures and sequence conservation that differ dramatically from authentic cellular tRNAs. This is mandated in part by the fact that they are part of the viral genome and are connected to it at their 5′ end; TLSs use a pseudoknot in place of the acceptor stem used in tRNA (Fig. 1A). However, TLSs have other secondary structure and sequence differences compared to tRNAs which may relate to the fact that they can play several roles during infection.

TLSs can alter the translation efficiency of an upstream open reading frame (ORF), but the mechanisms for this remain unknown (Barends et al. 2004; Matsuda and Dreher 2004; Rudinger-Thirion et al. 2006; Dreher 2010; Chujo et al. 2015; Hartwick et al. 2018). Viral proteins also interact with TLSs, which contain part or all of the viral negative-strand promoter site required for RNA-dependent RNA polymerase (RdRp) binding (Singh and Dreher 1997; Deiman et al. 1998; Osman et al. 2000; Olsthoorn et al. 2004; Yamaji et al. 2006; Rao and Cheng Kao 2015). In addition, in some viruses the TLS is essential for proper packaging of the virion, acting as a nucleation site for capsid assembly (Choi and Rao 2000; Choi et al. 2002). Thus, TLSs are multifunctional RNAs, a feature likely conferred by their three-dimensional structure, in particular the features that differ from authentic tRNA.

Studying TLSs may give insight into other types of tRNA mimics proposed to exist in viral and cellular RNAs, including the tRNA-miRNA-encoded RNAs (TMERs) in Gammaherpesvirus (Diebel et al. 2015) and those in some 3′ cap-independent translational enhancer (3′-CITE) elements (McCormack et al. 2008; Simon and Miller 2013). Nonviral tRNA mimics include transfer-messenger RNAs (tmRNAs) (Williams and Bartel 1995; Weis et al. 2010) and the MALAT1-derived mascRNA (Wilusz et al. 2008; Sun and Ma 2019; Lu et al. 2020). Notably, while some of these enhance translation, none are known to be aminoacylated and while some remain within the genome, others are processed out of the primary transcript. Thus, tRNA mimicry may be both useful and diverse, motivating efforts to understand how different types of tRNA mimicry are formed.

Three classes of TLSs are known: valine-accepting TLSs (TLS^{Val}), tyrosine-accepting TLSs (TLS^{Tyr}), and histidine-accepting TLSs (TLS^{His}) (Mans et al. 1991; Dreher 2010). Each class is distinct in the identity of the amino acid added to its 3′ end, secondary structure, and presumably

higher-order folding (Fig. 1B). All contain a pseudoknotted acceptor stem mimic as well as a 3′ CCA that is maintained on the viral genome by cellular processing machinery (Litvak et al. 1973; Dreher and Goodwin 1998; Osman et al. 2000). The TLS^{Val} class most resembles a canonical tRNA structure with discernible acceptor stem, D-arm, T-arm, and anticodon (AC)-arm elements (Pinck et al. 1970; Fukai et al. 2000; Hammond et al. 2009), confirmed by two x-ray crystal structures of the TYMV TLS (Colussi et al. 2014; Hartwick et al. 2018). Conversely, the TLS^{Tyr} class appears to be the most divergent from tRNAs, with several additional stem–loops, no clear T-arm or AC-arm, and thus no obvious way to mimic tRNA (Haenni et al. 1982; Dreher and Hall 1988; Felden et al. 1994a). However, a recent cryo-EM structure of the Brome mosaic virus (BMV) TLS^{Tyr} revealed tRNA mimicry is embedded in a more complex fold that may require programmed conformational changes to fully mimic tRNA (Bonilla et al. 2020).

The third class of TLSs, TLS^{His}, visually appears to lie between the other two in terms of structural similarity to canonical tRNA. The proposed TLS^{His} secondary structure has putative analogs to the AC-arm, T-arm, and acceptor stem, though it lacks an obvious D-arm analog (Ijberg and Philipson 1972; Salomon et al. 1976; Rietveld et al. 1984; Felden et al. 1996). High-resolution structural information on this class has remained elusive, likely due in part to structural heterogeneity as observed in the prototypical TLS^{His} RNA from the tobacco mosaic virus (TMV) (Hammond et al. 2009). Although structural modeling of the RNA provided insight into the possible TMV TLS three-dimensional fold (Rietveld et al. 1984; Felden et al. 1996), this model remains untested. Furthermore, only five TLS^{His} sequences have been identified, which makes analysis of this class challenging compared to the TLS^{Val} and TLS^{Tyr} classes (Dreher 2010; Sherlock et al. 2021; Bonilla et al. 2020). Hence, the TLS^{His} class represents a novel form of tRNA mimicry that can provide insight into diverse ways such mimicry can be achieved.

Previous studies identified 108 unique TLS^{Val} sequences (Sherlock et al. 2021) and 512 unique TLS^{Tyr} sequences (Bonilla et al. 2020), but only five examples of the TLS^{His} were known (Dreher 2010). This relative scarcity of sequence and structural information available for the TLS^{His} class motivated us to better understand how primary sequence, secondary structure, and tertiary contacts achieve the functionally required fold. Using the few previously reported TLS^{His} sequences, we performed bioinformatic searches based on primary sequence and secondary structure conservation to identify many additional putative TLS^{His} sequences. We used chemical probing to query the proposed secondary structures of some new TLS^{His} and used an in vitro aminoacylation assay to verify that they are functional, histidine-accepting TLSs. Finally, we interrogated a proposed D-loop mimic, implicating this region in a long-range interaction with the T-loop that may be analogous to the D-loop/T-loop interaction present in canonical tRNAs. Together, our findings uncover an expanded phylogenetic diversity of the TLS^{His} class and provide insight into how the structural conservation of these RNAs correlates with their tRNA mimicry.

RESULTS AND DISCUSSION

Bioinformatic searches reveal additional TLS^{His}

Identifying new TLS^{His} promised to reveal conserved regions required for achieving the structure, locations of possible protein interactions, and variations such as the insertions found in the divergent members of the TLS^{Val} and TLS^{Tyr} (Bonilla et al. 2020; Sherlock et al. 2021). To identify additional putative TLS^{His} RNAs, we used the program Infernal to perform homology-based searches (Nawrocki and Eddy 2013). We started with an initial seed alignment from the four TLS^{His} sequences deposited in the Rfam database (Rfam ID: RF01077) (Kalvari et al. 2018). This database seed alignment was incomplete, so we adjusted it to add the entire 3′ end, including the T-loop and acceptor stem pseudoknot. A search of all +ssRNA virus genomes deposited in the NCBI virus database identified 158 unique sequences from 36 unique viruses with substantial secondary structure conservation (Supplemental Files 1, 2). The difference between the number of unique sequences and unique viruses results from the presence of both genomic and subgenomic RNAs within a single viral species, and some sequence variations between isolates and strains (Adams et al. 2017). Of the 36 viruses containing a putative TLS^{His}, 33 belong to the *Tobamovirus* genus, two to the *Tymovirus* genus, and one to the *Furovirus* genus (Fig. 1C; Supplemental File 2), which are the genera previously known to contain TLS^{His}. Although the tobamoviruses and furoviruses are both in the *Virgaviridae* family and are closely related based on RdRp sequence, the tobamovirus TLS^{His} are more similar to those from the *Tymovirus* genus in the *Tymoviridae* family. The single TLS identified from *Furovirus* had a high E value of 0.019, making it an unlikely TLS^{His} candidate; rather, it demonstrates features of the TLS^{Val} class and was excluded from further analyses. Interestingly, the tymoviruses mostly contain TLS^{Val}, and most examples of TLS^{Val} are within *Tymoviridae*, with a few in *Virgaviridae* (Sherlock et al. 2021). While we cannot propose a specific evolutionary history of these viral lineages, this distribution suggests exchange of TLS elements between viruses during coinfections.

TLS^{His} RNAs adopt a conserved secondary structure

We calculated a consensus sequence and secondary structure model using CaCoFold with the 157 putative unique TLS^{His} sequences (Fig. 1D; Rivas et al. 2016, 2020). The

resultant covariation patterns strongly support the putative secondary structure of the prototypical TMV TLS^{His}. Specifically, both pseudoknots and analogs for the T-arm and AC-arm were present in our model and in good agreement with the observed base-pairing and covariation. Sequence conservation is markedly different in different regions of the secondary structure. Specifically, the sequence conservation is high in the acceptor stem analog PK1 and the T-arm analog (3′ region). The combined length of the T-arm plus PK1 is always 11 bp, 1 bp shorter than in the TLS^{Val} class (Sherlock et al. 2021). Within the T-arm, the T-loop is nearly perfectly conserved in TLS^{His} sequences, containing the 5′-UUCGAAU-3′ sequence common in tRNA T-loops. In fact, the T-loop of the TLS^{His} is more conserved than the T-loop of canonical tRNA^{His} (Westhof and Auffinger 2001). The conservation in this region likely reflects how these TLSs are recognized by proteins, including host HisRS, CCA-adding enzyme, and eEF1A, and viral RdRp (Hegg et al. 1990; Singh and Dreher 1997; Deiman et al. 1998; Osman et al. 2000; Zeenko et al. 2002; Olsthoorn et al. 2004; Yamaji et al. 2006; Hwang et al. 2013; Li et al. 2013). Indeed, key bases for recognition by host HisRS are in this region (Crothers et al. 1972; Hou 1997; Rudinger et al. 1997; Tian et al. 2015) and both the CCA-adding enzyme and eEF1A bind to this part of tRNAs (Nissen et al. 1995; Xiong and Steitz 2004).

In contrast to the 3′ region, the region comprising PK2 and the AC-arm analog (5′ region) exhibits substantial base-pair covariation but little primary sequence conservation, thus a specific secondary structure is required, largely independent of nucleotide identity. The exceptions are two isolated motifs that are conserved in sequence: the histidine AC (GUG) and a GG dinucleotide adjacent to PK2. Finally, we did not find any new TLS^{His} with substantial insertions or deletions as is seen in both the TLS^{Val} and TLS^{Tyr} classes (Bonilla et al. 2020; Sherlock et al. 2021). Cumulatively, these patterns suggest a conserved secondary structure present in histidine-accepting TLSs that matches the proposed structure of the archetypal TMV TLS^{His} and less global variation (insertions or deletions) than in the other TLS classes.

Chemical probing of individual TLS^{His} structures

While the high degree of covariation present in all base-pairing regions supports a common TLS^{His} secondary structure, experimental interrogation of representative RNAs is useful to test this and find patterns across the RNAs. We applied selective 2′ hydroxyl acylation analyzed by primer extension (SHAPE) in vitro chemical probing, which queries the conformational flexibility at each nucleotide position in an RNA (Yoon et al. 2011; Kim et al. 2013; Cordero et al. 2014; Kladwang et al. 2014; Lee et al. 2015). Locations in the RNA that are more conformationally dynamic, such as in unpaired bases, react more readily with the SHAPE reagent *N*-methyl isatoic anhydride (NMIA) than those in interactions that restrict motion, such as in base pairs. We applied this method to the known TLS^{His} from Tobacco Mosaic Virus (TMV) and putative TLS^{His}s from Odontoglossum Ringspot Virus (ORSV), Ribgrass Mosaic Virus (RMV), Cucumber Mottle Virus (CMoV), Maracuja Mosaic Virus (MarMV), Hibiscus Latent Fort Pierce Virus (HLFPV), Zucchini Green Mottle Mosaic Virus (ZGMMV), and Diascia Yellow Mottle Virus (DiaYMV). Mapping reactivities onto the secondary structure models, we observed patterns consistent with each proposed secondary structure (Fig. 2; Supplemental Fig. S1). Specifically, low reactivities were observed in regions proposed to be base-paired, namely both pseudoknot regions, the AC stem, and the T-arm stem. Conversely, most regions predicted to lack canonical base-pairing in the model contained elevated levels of reactivity: the AC loop, the linker regions following PK2, the T-loop, and the CCA trinucleotide. Additionally, the internal loop or bulge present in all AC stems was highly reactive, consistent with conformational dynamics in this region. This loop often contains 5 nt but varies in size (Fig. 2; Supplemental Fig. S1). Notably, some base-paired regions exhibited some chemical reactivity, such as part of the AC stem and the 3 bp stem in PK1. This likely indicates some degree of local conformational dynamics or specific reactive structural features that allow modification by the reagent.

Representative putative new TLS^{His} are histidylated in vitro

While all new putative TLS^{His} conformed to the consensus secondary structure, the sequence diversity motivated us to qualitatively test their ability to be aminoacylated by histidyl-tRNA synthetase (HisRS). We used in vitro aminoacylation assays with purified HisRS from *S. cerevisiae* and *N. tabacum* (Supplemental Fig. S2), and ^{3}H-2,5-*L*-histidine as substrate. We first tested the specificity of these enzymes with yeast histidine tRNA (tRNA^{His}) and a yeast leucine tRNA (tRNA^{Leu}) as positive and negative controls, respectively. With both HisRS enzymes, the yeast tRNA^{His} was histidylated to a high level while yeast tRNA^{Leu} showed levels similar to a reaction with no RNA (Fig. 3A, B). We then tested both enzymes using the TYMV TLS^{Val}, as previous studies show TYMV may be histidylated, likely due to a nucleotide within the acceptor stem pseudoknot that mimics the −1 base in a tRNA^{His} (Dreher and Goodwin 1998). These experiments recapitulate the finding that the TMYV TLS^{Val} can be histidylated to some degree by the *S. cerevisiae* HisRS but not *N. tabacum* HisRS (Fig. 3A,B).

Under these conditions, the prototypical TLS^{His} from TMV was histidylated at levels matching or exceeding tRNA^{His} with either enzyme (Fig. 3A,B; Felden et al. 1994b). We then tested seven representative newly identified putative TLS^{His} RNAs, chosen to contain variable

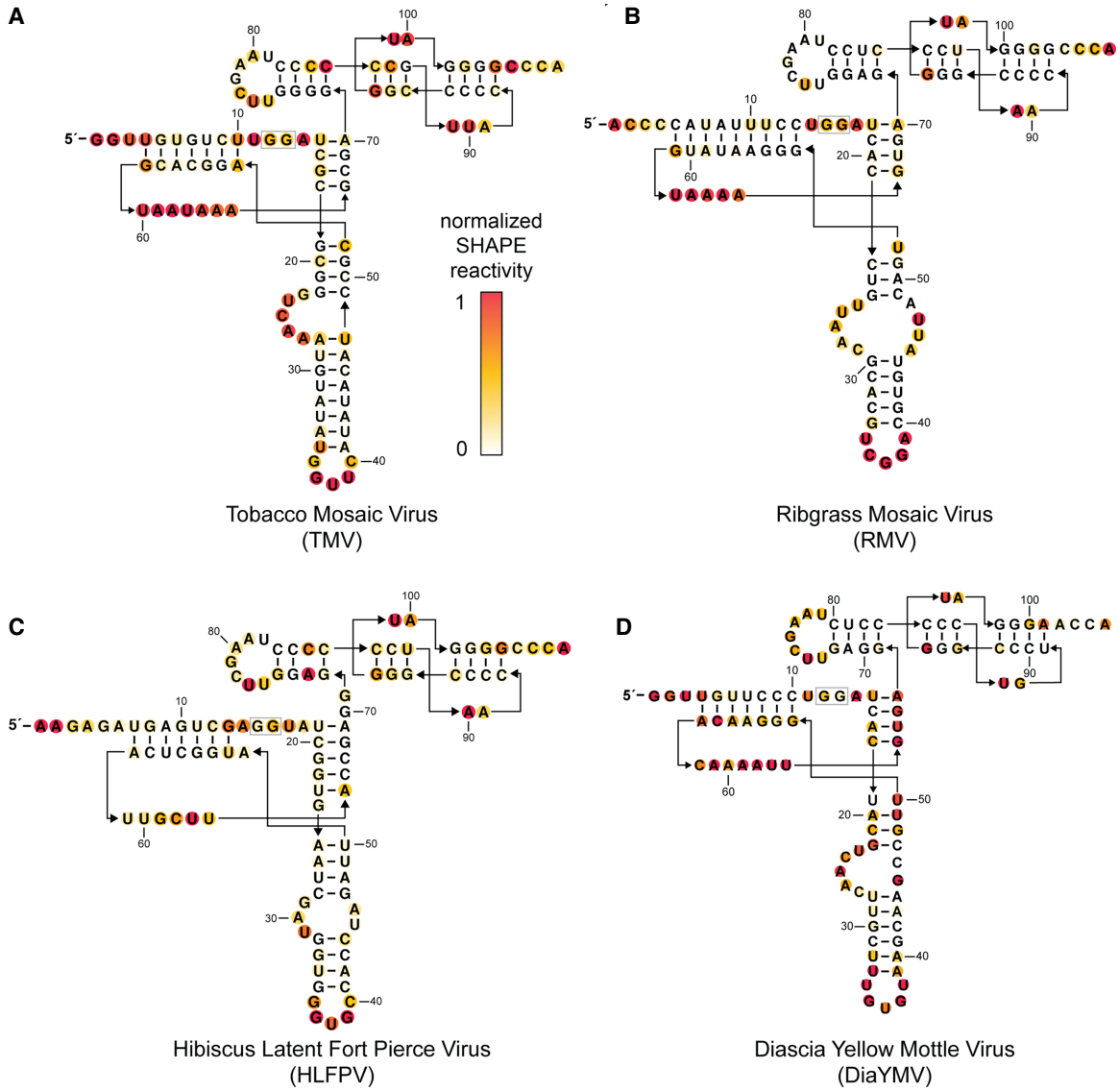

FIGURE 2. Histidine-accepting tRNA-like structures adopt a conserved secondary structure. Chemical probing of four representative TLS^{His} RNAs using the SHAPE reagent NMIA: (*A*) Tobacco Mosaic virus, (*B*) Ribgrass Mosaic virus, (*C*) Hibiscus Latent Fort Pierce virus, and (*D*) Diascia Yellow Mottle virus. Reactivity was background subtracted and normalized to flanking 5′ and 3′ normalization hairpins (not depicted; see Supplemental File 2 for sequence details). Coloring represents degree of normalized modification according to the inset legend.

features including diverse anticodon sequences, discriminator nucleotide identity, AC stem length, and AC bulge size. All of these putative TLS^{His} RNAs were histidylated well above the negative controls by both the yeast and tobacco HisRS (Fig. 3A,B). In addition to the endpoint experiments described here using substrate levels of enzyme, we performed an enzyme titration with ORSV demonstrating this histidylation was not an artifact of the high enzyme concentration (Supplemental Fig. S2C). Although we did not test every new putative TLS^{His}, the fact that all those that were tested were aminoacylated, and the robust conservation within the class, suggests that most are likely functional substrates for HisRS.

TLS^{His} aminoacylation bypasses features required in tRNAs

Several important identity nucleotides that facilitate recognition by HisRS appear in TLS^{His} RNAs (Rudinger et al. 1997; Dreher 2010), but also several TLS^{His} that lacked these features were aminoacylated (Fig. 3A,B). Specifically, two important tRNA^{His} identity elements are the N_{-1} and N_{73} bases at the end of the acceptor stem (Rudinger et al. 1997; Tian et al. 2015). These are nearly invariant across tRNA^{His} as G_{-1} and A_{73}. However, in TLS^{His} the homologous bases are often an A at N_{-1} and a C at N_{73} (Fig. 1D), with some variation. Our results suggest the discriminator

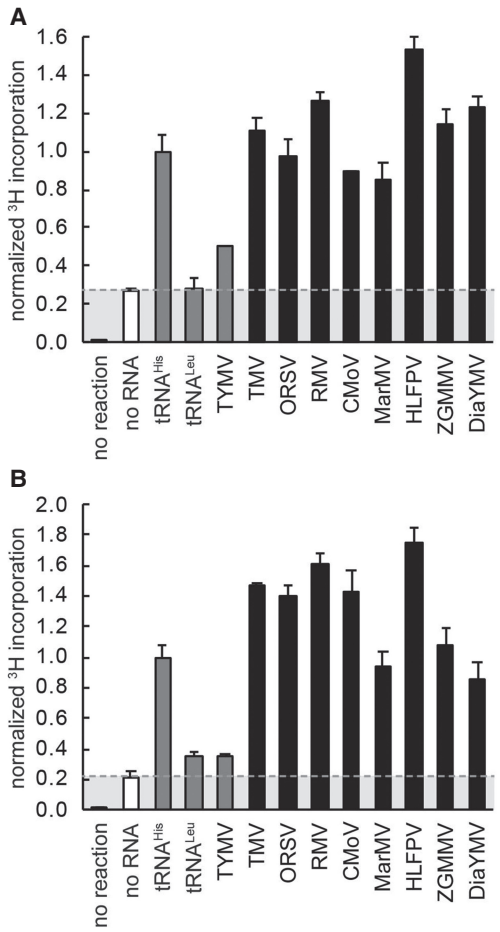

FIGURE 3. Identified putative viral TLS^{His} sequences are histidylated in vitro. ^{3}H-L-histidine incorporation of eight representative TLS^{His} RNAs identified through bioinformatic searches. Histidylation of each RNA, as measured by covalent incorporation of ^{3}H-L-histidine by (*A*) *S. cerevisiae* histidine tRNA-synthetase and (*B*) *N. tabacum* histidine tRNA-synthetase at the 3′ adenosine, is normalized to yeast tRNA^{His} RNA. The dashed line and shaded region indicate the background of a reaction containing no RNA. Each reaction was performed in triplicate. Error bars represent one standard error from the mean.

nucleotide is not always essential for histidylation for TLS^{His}, as there was no significant decrease in histidine incorporation for DiaYMV, which contains an A at position 73 in place of the C typical of most TLS^{His} and many tRNA^{His}; experiments measuring k_{cat}/K_M will be useful to fully understand quantitative effects of this nucleotide on aminoacylation levels. Notably, in most members of the *Virgaviridae* family the discriminator nucleotide analog N_{73} is a C and in all members of the *Tymoviridae* family it is an A. It appears that rather than reflecting the identity of the canonical discriminator nucleotide, this base reflects the viral RdRp lineage (Deiman et al. 1998; Osman et al. 2000), which appears to also be true in the TLS^{Val} class (Sherlock et al. 2021). Of similar note is the lack of the −1 G found in histidine tRNAs. During processing of the immature tRNA^{His}, the enzyme tRNA^{His} guanylyltransferase (THG1) and homologs covalently attach a guanine base to the 5′ end of the tRNA that is recognized by the host HisRS during aminoacylation. Because TLSs are found at the 3′ end of the viral genome there is no available 5′ end for THG1 to modify. Previous studies have suggested an A within the acceptor stem pseudoknot may accomplish a similar function (Fig. 1D; labeled as N_{-1}; Rudinger et al. 1994), making TLS^{His} THG1-independent.

The other important identity element within tRNA^{His} is the AC loop; in the TLS^{His} it is most often a GUG as in canonical tRNA^{His} (Rudinger et al. 1997). However, exceptions to this, namely TMV (GUU), RMV (CGG), and MarMV (AGA) TLSs, were readily aminoacylated (Fig. 3A,B). Of note, the TLS^{His} AC loop is not as well conserved as in the TLS^{Val} class where the sequence is critical for aminoacylation (Sherlock et al. 2021). Additionally, the TLS^{His} AC loop is predicted to contain 5 nt with covariation in the stem's terminal base pair, contrasting with the canonical 7 nt tRNA^{His} AC loop (Rudinger et al. 1997). Finally, in the TLS^{His}, the AC stem always contains an internal loop or bulge and is significantly longer than the AC stem of the TLS^{Val} class. This difference likely relates to the three-dimensional structure of the TLS^{His} RNAs, though further studies are needed. Perhaps the flexibility in this region affords the structure with dynamic capabilities to switch between different functional states, as proposed for the TLS^{Tyr} (Bonilla et al. 2020); this could explain previous data suggesting conformational heterogeneity in TLS^{His} samples (Hammond 2009).

Evidence for a conserved D-loop/T-loop-like interaction in the TLS^{His}

Chemical probing showed that in several TLS^{His}, the conserved GG dinucleotides present between PK2 and the AC stem had decreased reactivity compared to adjacent nucleotides and other unpaired regions, despite no obvious base-pairing partners (Fig. 2). Similarly, the T-loop region displayed decreased levels of SHAPE reactivity when compared with other loop and linker regions. Within the T-loop, the pattern is similar to what is observed in canonical tRNAs; the second U was consistently more reactive than the rest of the loop (Kladwang et al. 2011). In canonical tRNAs this elevated reactivity is due to the unique local backbone geometry (Kladwang et al. 2011; Tian et al. 2015), which facilities an interaction with the D-loop, forming the tRNA "elbow" (Levitt 1969; Rould et al. 1989; Tian et al. 2015). The similar reactivity pattern in TLS^{His} suggests a similar structure in the TLS^{His} T-loop, that then could interact with the conserved GG dinucleotide, as previously proposed but not directly tested (Felden et al. 1996).

To test if the TLS^{His} class contains an interaction between the conserved GG dinucleotide and the T-loop, we assessed the functional and structural effects of mutating these elements. First, we individually introduced

a G → A mutation in the GG dinucleotide proposed to interact with the T-loop, or a C → U mutation in the T-loop, in three representative RNAs: TMV, RMV, and DiaYMV TLS^{His} (Fig. 4A,B). Analogous mutations in tRNAs, G19A and C56U, disrupt the D-loop/T-loop interaction, resulting in decreased aminoacylation (Du and Wang 2003). When the G → A and C → U mutants were tested in several TLS^{His}, all exhibited decreased levels of aminoacylation relative to WT (Fig. 4C,D). Although a double mutant of the TMV TLS containing both the G13A and C77U mutations might be expected to restore activity, in fact similar compensatory mutations do not restore activity in canonical tRNAs (Du and Wang 2003). This is not surprising given the structural context of the T-loop and the nature of the long-range interactions. Consistent with this, the G → A + C → U double mutants also did not restore aminoacylation in the TMV TLS^{His} (Supplemental Fig. S3A,B). Overall, the near total loss of histidine incorporation resulting from these mutations is similar to what has been observed for canonical tRNAs when the T-loop/D-loop interaction is disrupted (Du and Wang 2003).

The aminoacylation assays reveal the functional importance of the T-loop and GG nucleotides but do not show if they interact, so we used chemical probing to determine if mutation to either induced changes in other parts of the RNA. SHAPE probing of the C → U RNAs revealed substantial increases in reactivity in the T-loop, consistent with destabilization of the loop's structure (Fig. 4A,B). In addition, the C → U mutation increased reactivity of the GG dinucleotides, while changes in the rest of the RNA were minimal (Supplemental Fig. S4). Thus, disruption of the T-loop in these TLS^{His} causes local structural changes in the GG dinucleotide, consistent with a long-range interaction between these elements. The G → A mutation in the GG dinucleotide induced increased reactivity in the GG dinucleotide and some subtle increases in the T-loop (Fig. 4A,B). This is consistent with the proposed interaction and likely reflects the fact that the T-loop comprises a preformed structural motif whose structure is less dependent on tertiary interactions (Chan et al. 2013).

Our data suggest that the GG dinucleotide between PK2 and the AC stem of TLS^{His} acts analogously to the D-loop in tRNAs, making a specific long-range contact to the T-loop as previously proposed (Felden et al. 1996). Although high-resolution structural data will be needed to verify this interaction, we speculate there is a Watson–Crick base pair between the first G of the dinucleotide, G_{12} in our TMV construct, and the third base in the T-loop, C_{78}, as well as the reverse Hoogsteen base pair between G_{13} and U_{76}, as seen in tRNAs (Supplemental Fig. S3C,D). In tRNAs this interaction is critical to create the functional global fold; the GG dinucleotide "D-loop"/T-loop interaction in

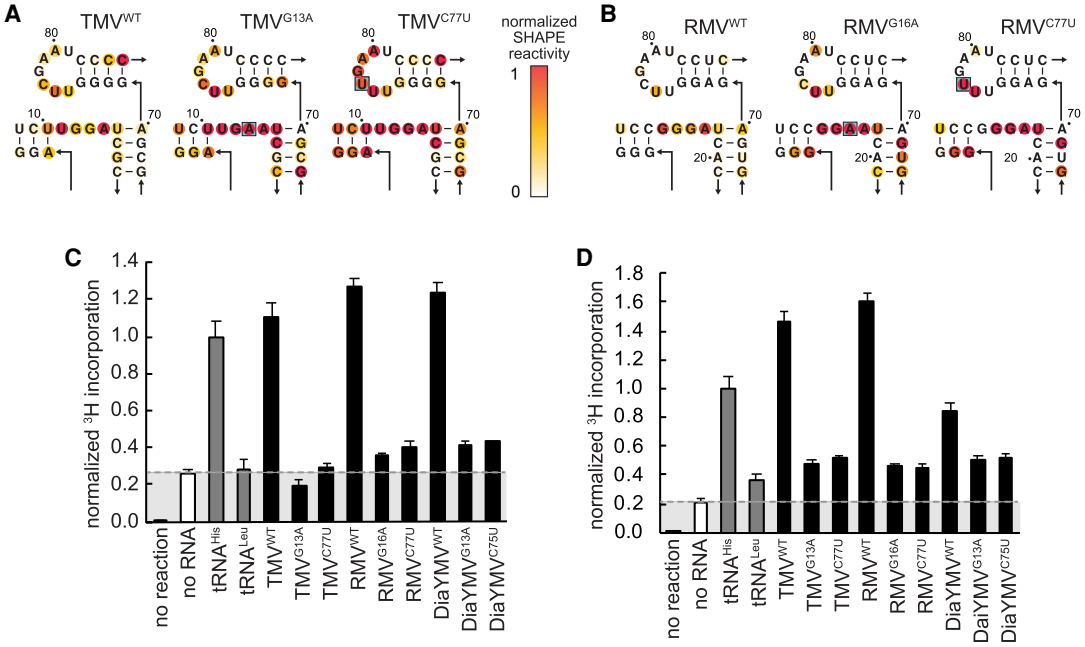

FIGURE 4. A putative D-loop/T-loop mimic is required for structure and efficient histidylation. (*A*,*B*) SHAPE chemical probing of the wild-type TMV (*A*) and RMV (*B*) TLSs and two D-loop/T-loop mutants (boxed in figure). Reactivity was background subtracted and normalized to flanking 5′ and 3′ normalization hairpins (not shown). (*C*) ^{3}H-L-histidine incorporation using *S. cerevisiae* HisRS of three representative TLS^{His} RNAs; TMV, RMV, and DiaYMV, each with the wild-type sequence as well as two D-loop/T-loop mutants. Histidylation of each RNA, as measured by covalent incorporation of ^{3}H-L-histidine by histidine tRNA-synthetase (HisRS), is normalized to yeast tRNA^{His}. The dashed line and shaded region indicate the background of a reaction containing no RNA. (*D*) As in *C*, but with *N. tabacum* HisRS. Each reaction was performed in triplicate. Error bars represent one standard error from the mean.

TLS^{His} may play a similar structural and functional role, positioning the AC stem and acceptor pseudoknot such that the HisRS can productively recognize these elements. Additionally, within the T-loop several nucleotides are modified in tRNAs and have been shown to be modified in the analogous region of Brome Mosaic Virus (Baumstark and Ahlquist 2001); whether similar modifications are present within members of the TLS^{His} class remains to be explored.

Comparisons between the TLS^{His} and other TLS classes

In some ways, characteristics of the TLS^{His} class lie in the middle of the three known TLS classes. For example, the identity and size of the AC loop is strictly conserved for TLS^{Val}, and examples that lack a valine anticodon are not aminoacylated by valyl-tRNA synthetase (Dreher et al. 1992; Sherlock et al. 2021). In contrast, the AC loop is not conserved for the TLS^{Tyr} class, to the point where there are disagreements in its identity (Perret et al. 1989; Felden et al. 1994a; Bonilla et al. 2020). While many TLS^{His} representatives contain a GUG histidine AC, there are examples that do not, and the AC loop length for TLS^{His} is typically only five instead of seven nucleotides. Additionally, the TLS^{His} class contains more secondary structure elements than TLS^{Val} and fewer than TLS^{Tyr} and also falls in the middle in average length. Perhaps this intermediate status could help elucidate the evolutionary relationship and trajectory of the different TLS classes. While our current studies do not address these evolutionary relationships, it is noteworthy that the TLS^{His} and TLS^{Val} structures have enough similarity, especially in the 3′ regions, that bioinformatic searches based on the TLS^{His} class can find TLS^{Val} and vice versa, albeit mostly at E values above the inclusion threshold (Sherlock et al. 2021). It also remains to be determined how the TLSs achieve specificity for a particular amino acid given the observed diversity in identity elements. It is intriguing to speculate that other classes of TLSs exist that are structurally unique compared to the three known classes. There is certainly precedent to support this, given the constantly expanding list of classes of riboswitches, ribozymes, and xrRNAs as well as the existence of other tRNA-mimicking structures such as TMERs, tmRNAs, and mascRNAs.

Concluding remarks

In this study, we expanded the list of known TLS^{His}, confirmed their shared secondary structure, shown they are histidylated in vitro and provided evidence for a proposed D-loop/T-loop interaction analog. These discoveries present new questions regarding how this class of TLSs achieves specific interactions required for recognition by both host and viral proteins while demonstrating significant sequence and secondary structure variation from canonical tRNAs. While the experiments and analyses herein build on and confirm previous observations and hypotheses regarding TLS^{His}, high-resolution structural information on TLS^{His} RNAs will be necessary to address lingering questions regarding their structure and function. For example, in this class the AC-arm is particularly long compared to canonical $tRNA^{His}$ and always has an internal loop. How this additional length is accommodated, if the loop affects orientation of the anticodon relative to a bound HisRS, and if these elements provide conformational dynamics or reconfigurations remains to be understood. Overall, this study moves us closer to understanding the molecular interactions underlying tRNA mimicry for the TLS^{His} class in terms of structure, while the overall topology, intermolecular interactions with host and viral proteins, and ultimately the function of these RNA elements during infection, remain to be elucidated.

MATERIALS AND METHODS

TLS^{His} bioinformatic searches and consensus model generation

An alignment of four known histidine-accepting tRNA like structures (TLS^{His}) (Rfam ID: RF01077) was obtained from the Rfam database (Kalvari et al. 2018) and extended to include the entire TLS, as the existing alignment ended prior to the T-loop and PK1. Using Infernal version 1.1 (Nawrocki and Eddy 2013) a database consisting of all +ssRNA virus sequences deposited in the National Center for Biotechnology Information (NCBI, retrieved 01/22/2019) was queried to identify additional instances of this motif. Sequences identified by Infernal were added to the initial four sequences to generate an updated covariance model for subsequent iterative searching. Only sequences below the Infernal E-value threshold of 0.05 were considered. Duplicate sequences were removed, yielding 158 sequences from 36 unique viruses. A TLS identified from *Furovirus* with a high E value of 0.019, making it an unlikely TLS^{His} candidate, was removed, as it demonstrated features of the TLS^{Val} class and previously was identified with high confidence as a member of this class (Sherlock et al. 2021). Thus it was excluded from further analyses, resulting in 157 sequences from 35 unique viruses. These resulting sequences were used to generate a consensus sequence and secondary structure model including an analysis of covariance using the RNA Covariation Above Phylogenetic Expectation CaCoFold (R-scape v1.5.16) (Rivas et al. 2016, 2020) then rendered in R2R (Weinberg and Breaker 2011).

Expression of *Saccharomyces cerevisiae* HisRS

The DNA sequence encoding the HisRS enzyme from *S. cerevisiae* (GenBank: AJW07132.1) was purchased as a dsDNA gBlock (IDT) and cloned into a pET15b(+) vector containing an in-frame amino-terminal hexahistidine affinity tag. The protein was recombinantly expressed in BL21 (DE3) cells. Cells were grown in LB to an OD_{600} of 0.3, then protein expression was induced using 250 μM isopropyl β-D-1-thiogalactopyranoside (IPTG) overnight

at 18°C. Pelleted cells were resuspended in lysis buffer containing 20 mM Tris-HCl (pH 7.0), 500 mM NaCl, 2 mM β-mercaptoethanol (BME), 10% (v/v) glycerol, and cOmplete EDTA-free protease inhibitor cocktail tablets (Roche). Cell lysate was then sonicated on ice for 2 min of: 20 sec on, 40 sec off at 75 W. Cell lysate was clarified by centrifugation at 30,000*g* for 30 min at 4°C. The soluble fraction was purified by nickel affinity chromatography in a buffer containing 150 mM NaCl, 20 mM Tris-HCl (pH 7.0), 200 mM imidazole, 10% glycerol, and 2 mM β-mercaptoethanol. The protein was exchanged into a storage buffer containing 50 mM Tris-HCl (pH 8.0), 100 mM NaCl, 5 mM $MgCl_2$, and 5% glycerol using a spin concentrator (Amicon) and stored at 0.3 mg mL^{-1} at −80°C with working stocks stored at −20°C.

Expression of *Nicotiana tabacum* HisRS

The DNA sequence encoding the HisRS enzyme from *N. tabacum* (NCBI Reference Sequence: XP_016505768.1) in a pET15b(+) vector was purchased (Gene Universal). The protein was purified in the same manner as above, with a subsequent size exclusion step in a buffer containing 50 mM Tris-HCl (pH 8.0), 100 mM NaCl, and 5 mM $MgCl_2$. The protein was exchanged into a storage buffer containing 50 mM Tris-HCl (pH 8.0), 100 mM NaCl, 5 mM $MgCl_2$, and 5% glycerol using a spin concentrator (Amicon) and stored at 1.3 mg mL^{-1} at −80°C with working stocks stored at −20°C.

In vitro RNA transcription

DNA templates were ordered as gBlock DNA fragments (IDT) and cloned into pUC19. An amount of 200 µL PCR reactions using primers containing an upstream T7 promoter were used to generate dsDNA templates for transcription. Typical PCR conditions: 100 ng plasmid DNA, 0.5 µM forward and reverse DNA primers (Supplemental File 2), 500 µM dNTPs, 25 mM TAPS-HCl (pH 9.3), 50 mM KCl, 2 mM $MgCl_2$, 1 mM β-mercaptoethanol, and Phusion DNA polymerase (New England BioLabs). Templates for RNA used in aminoacylation assays were amplified using reverse primers containing two 5′-terminal 2′-*O*-methyl modified bases to ensure the correct 3′ end of the RNA. dsDNA amplification was confirmed by 1.5% agarose gel electrophoresis. Transcriptions were performed in 1 mL volume using 200 µL of PCR product (~0.1 µM template DNA) and 10 mM NTPs, 75 mM $MgCl_2$, 30 mM Tris-HCl (pH 8.0), 10 mM DTT, 0.1% spermidine, 0.1% Triton X-100, and T7 RNA polymerase. Reactions were incubated at 37°C overnight. After transcription, insoluble inorganic pyrophosphate was removed by centrifugation at 5000*g* for 5 min, then the RNA-containing supernatant was ethanol precipitated with three volumes of 100% ethanol at −80°C for a minimum of 1 h and then centrifuged at 21,000*g* for 30 min at 4°C to pellet the RNA, and the ethanolic fraction was decanted. The RNA was resuspended in 9 M urea loading buffer then purified by denaturing 10% PAGE. Bands were visualized by UV shadowing then excised. Bands were then crush-soaked in diethylpyrocarbonate-treated (DEPC) milli-Q water at 4°C overnight. The RNA-containing supernatant was then concentrated using spin concentrators (Amicon) to the appropriate concentration in DEPC-treated water. RNAs were stored at −80°C with working stocks stored at −20°C.

In vitro chemical probing of RNAs

Structure probing experiments using the SHAPE reagent NMIA were performed as described previously (Cordero et al. 2014). Briefly, 240 µM RNA was refolded by heating to 90°C for 5 min, cooled to ambient temperature, then incubated at ambient temperature with $MgCl_2$ for 20 min. Subsequently, the refolded RNA was modified by incubating with NMIA for 15 min at ambient temperature. NMIA modification conditions: 120 nM RNA, 6 mg/mL NMIA or DMSO, 50 mM HEPES-KOH (pH 8.0), 10 mM $MgCl_2$, 3 nM 6-fluorescein amidite 5′-labeled FAM-RT primer (Supplemental File 2). Modification was quenched by the addition of NaCl to 500 mM, Na-MES buffer (pH 6.0) to 50 mM, and oligo (dT) magnetic beads [Invitrogen Poly(A) Purist MAG Kit]. Modified RNAs were recovered using the magnetic beads, washed twice with 70% ethanol, then resuspended in water. Reverse transcription was carried out using SuperScript III (Invitrogen) at 48°C for 1 h per the manufacturer's instructions. The RNA was then degraded by the addition of NaOH to 200 mM and heating to 90°C for 5 min. An acid-quench solution (final concentration: 250 mM NaOAc [pH 5.2], 250 mM HCl, 500 mM NaCl) was added and DNA was recovered using the magnetic beads. The DNA was washed twice with 70% ethanol and eluted in GeneScan 350 ROX Dye Size Standard (ThermoFisher) containing HiDi formamide solution (ThermoFisher). 5′-FAM-labeled reverse-strand DNA products were resolved by capillary electrophoresis using an Applied Biosystems 3500 XL instrument. Data workup was performed using the HiTrace RiboKit (https://ribokit.github.io/HiTRACE/) (Yoon et al. 2011; Kim et al. 2013; Kladwang et al. 2014; Lee et al. 2015) in MatLab (MathWorks), and figures were rendered using RiboPaint (https://ribokit.github.io/RiboPaint/) in MatLab, then labeled in Adobe Illustrator. SHAPE reactivity was superimposed on the predicted secondary structure and used to make adjustments to the secondary structure model.

In vitro aminoacylation assays

Aminoacylation constructs were refolded by heating to 90°C for 5 min then cooling to ambient temperature, then incubated with 10 mM $MgCl_2$ for 20 min. Aminoacylation reactions were set up as follows: 1 µL of 1 µM RNA or water, 1 µL of freshly prepared aminoacylation buffer (10×: 200 mM HEPES-KOH [pH 7.5], 20 mM ATP, 300 mM KCl, 50 mM $MgCl_2$, 50 mM DTT), 1 µL of ^{3}H-2,5-L-histidine, 6 µL of DEPC-treated water, and 1 µL of HisRS (3 µM). Aminoacylation reactions were incubated at 30°C for 2 h. Reactions were quenched with 100 µL of wash buffer (20 mM Bis-Tris [pH 6.5], 10 mM NaCl, 1 mM $MgCl_2$) with trace xylene cyanol for visualization. Quenched reactions were immediately loaded onto a vacuum filter blotting apparatus. Filter stack in order from top to bottom: 0.45 µM Tuffryn membrane filter paper (PALL Life Sciences), HyBond positively charged membrane (GE Healthcare), thick filter paper (Bio-Rad gel dryer filter paper). Prior to filter blotting apparatus assembly, each layer was equilibrated in wash buffer. After application of the reaction solution, each blot was immediately washed with 3 × 300 µL of wash buffer containing trace xylene cyanol. The filters were subsequently dried and the blots from the HyBond membrane were excised and measured for ^{3}H incorporation by liquid scintillation counter (Perkin-Elmer Tri-Carb 2910 TR). Data processing was performed in Excel.

SUPPLEMENTAL MATERIAL

Supplemental material is available for this article.

ACKNOWLEDGMENTS

The authors thank the members of the Kieft laboratory for thoughtful discussions and David Costantino for critical reading of this manuscript. This work was supported by National Institutes of Health (NIH) grant R35GM118070 to J.S.K. M.E.S. is a Jane Coffin Childs Postdoctoral Fellow.

Received December 3, 2020; accepted March 30, 2021.

REFERENCES

Adams MJ, Adkins S, Bragard C, Gilmer D, Li D, MacFarlane SA, Wong SM, Melcher U, Ratti C, Ryu KH. 2017. ICTV virus taxonomy profile: *Virgaviridae*. *J Gen Virol* **98:** 1999–2000. doi:10.1099/jgv.0.000884

Barends S, Rudinger-Thirion J, Florentz C, Giegé R, Pleij CWA, Kraal B. 2004. tRNA-like structure regulates translation of brome mosaic virus RNA. *J Virol* **78:** 4003–4010. doi:10.1128/JVI.78.8.4003-4010.2004

Baumstark T, Ahlquist P. 2001. The brome mosaic virus RNA3 intergenic replication enhancer folds to mimic a tRNA TΨC-stem loop and is modified in vivo. *RNA* **7:** 1652–1670.

Bonilla S, Sherlock ME, Macfadden A, Kieft JS. 2020. A structured viral RNA uses molecular mimicry and conformational dynamics to coordinate multiple functions. bioRxiv doi:10.1101/2020.09.18.302638.

Chan CW, Chetnani B, Mondragón A. 2013. Structure and function of the T-loop structural motif in noncoding RNAs. *Wiley Interdiscip Rev RNA* **4:** 507–522. doi:10.1002/wrna.1175

Choi YG, Rao ALN. 2000. Packaging of Tobacco mosaic virus subgenomic RNAs by Brome mosaic virus coat protein exhibits RNA controlled polymorphism. *Virology* **275:** 249–257. doi:10.1006/viro.2000.0532

Choi YG, Dreher TW, Rao ALN. 2002. tRNA elements mediate the assembly of an icosahedral RNA virus. *Proc Natl Acad Sci* **99:** 655–660. doi:10.1073/pnas.022618199

Chujo T, Ishibashi K, Miyashita S, Ishikawa M. 2015. Functions of the 5′- and 3′-untranslated regions of tobamovirus RNA. *Virus Res* **206:** 82–89. doi:10.1016/j.virusres.2015.01.028.

Colussi TM, Costantino DA, Hammond JA, Ruehle GM, Nix JC, Kieft JS. 2014. The structural basis of transfer RNA mimicry and conformational plasticity by a viral RNA. *Nature* **511:** 366–369. doi:10.1038/nature13378

Cordero P, Kladwang W, VanLang CC, Das R. 2014. The mutate-and-map protocol for inferring base pairs in structured RNA. *Methods Mol Biol* **1086:** 53–77. doi:10.1007/978-1-62703-667-2_4

Crothers DM, Seno T, Söll G. 1972. Is there a discriminator site in transfer RNA? *Proc Natl Acad Sci* **69:** 3063–3067. doi:10.1073/pnas.69.10.3063

Deiman BALM, Koenen AK, Verlaan PWG, Pleij CWA. 1998. Minimal template requirements for initiation of minus-strand synthesis in vitro by the RNA-dependent RNA polymerase of turnip yellow mosaic virus. *J Virol* **72:** 3965–3972. doi:10.1128/JVI.72.5.3965-3972.1998

Diebel KW, Oko LM, Medina EM, Niemeyer BF, Warren CJ, Claypool DJ, Tibbetts SA, Cool CD, Clambey ET, van Dyk LF. 2015. Gammaherpesvirus small noncoding RNAs are bifunctional elements that regulate infection and contribute to virulence in vivo. *MBio* **6:** 1–15. doi:10.1128/mBio.01670-14

Dreher TW. 2010. Viral tRNAs and tRNA-like structures. *Wiley Interdiscip Rev RNA* **1:** 402–414. doi:10.1002/wrna.42

Dreher TW, Goodwin JB. 1998. Transfer RNA mimicry among tymoviral genomic RNAs ranges from highly efficient to vestigial. *Nucleic Acids Res* **26:** 4356–4364. doi:10.1093/nar/26.19.4356

Dreher TW, Hall TC. 1988. Mutational analysis of the tRNA mimicry of brome mosaic virus RNA. Sequence and structural requirements for aminoacylation and 3′-adenylation. *J Mol Biol* **201:** 41–55. doi:10.1016/0022-2836(88)90437-8

Dreher TW, Tsai CH, Florentz C, Giegé R. 1992. Specific valylation of turnip yellow mosaic virus RNA by wheat germ valyl-tRNA synthetase determined by three anticodon loop nucleotides. *Biochemistry* **31:** 9183–9189. doi:10.1021/bi00153a010

Dreher TW, Uhlenbeck OC, Browning KS. 1999. Quantitative assessment of EF-1α · GTP binding to aminoacyl-tRNAs, aminoacyl-viral RNA, and tRNA shows close correspondence to the RNA binding properties of EF-Tu. *J Biol Chem* **274:** 666–672. doi:10.1074/jbc.274.2.666

Du X, Wang ED. 2003. Tertiary structure base pairs between D- and TΨC-loops of *Escherichia coli* $tRNA^{Leu}$ play important roles in both aminoacylation and editing. *Nucleic Acids Res* **31:** 2865–2872. doi:10.1093/nar/gkg382

Felden B, Florentz C, Giegé R, Westhof E. 1994a. Solution structure of the 3′-end of brome mosaic virus genomic RNAs: conformational mimicry with canonical tRNAs. *J Mol Biol* **235:** 508–531. doi:10.1006/jmbi.1994.1010

Felden B, Florentz C, Mcpherson A, Giegé R. 1994b. A histidine accepting tRNA-like fold at the 3′-end of satellite tobacco mosaic virus RNA. *Nucleic Acids Res* **22:** 2882–2886. doi:10.1093/nar/22.15.2882

Felden B, Florentz C, Giegé R, Westhof E. 1996. A central pseudoknotted three-way junction imposes tRNA-like mimicry and the orientation of three 5′ upstream pseudoknots in the 3′ terminus of tobacco mosaic virus RNA. *RNA* **2:** 201–212.

Fukai S, Nureki O, Sekine S, Shimada A, Tao J, Vassylyev DG, Yokoyama S. 2000. Structural basis for double-sieve discrimination of L-valine from L-isoleucine and L-threonine by the complex of tRNA(Val) and valyl-tRNA synthetase. *Cell* **103:** 793–803. doi:10.1016/S0092-8674(00)00182-3

Gamarnik A V, Andino R. 1998. Switch from translation to RNA replication in a positive-stranded RNA virus. *Genes Dev* **12:** 2293–2304. doi:10.1101/gad.12.15.2293

Garcia-Blanco MA, Vasudevan SG, Bradrick SS, Nicchitta C. 2016. Flavivirus RNA transactions from viral entry to genome replication. *Antiviral Res* **134:** 244–249. doi:10.1016/j.antiviral.2016.09.010.

Goodwin JB, Dreher TW. 1998. Transfer RNA mimicry in a new group of positive-strand RNA plant viruses, the furoviruses: differential aminoacylation between the RNA components of one genome. *Virology* **246:** 170–178. doi:10.1006/viro.1998.9193

Haenni A-L, Joshi S, Chapevil F. 1982. tRNA-like structures in the genomes of RNA viruses. *Prog Nucleic Acid Res Mol Biol* **27:** 85–104. doi:10.1016/S0079-6603(08)60598-X

Hammond JA. 2009. *A survey of tRNA mimicry: structural studies of plant viral RNA elements and their role in viral processes*. https://search.proquest.com/docview/220297257?accountid=12834.

Hammond JA, Rambo RP, Filbin ME, Kieft JS. 2009. Comparison and functional implications of the 3D architectures of viral tRNA-like structures. *RNA* **15:** 294–307. doi:10.1261/rna.1360709

Hartwick EW, Costantino DA, MacFadden A, Nix JC, Tian S, Das R, Kieft JS. 2018. Ribosome-induced RNA conformational changes in a viral 3′-UTR sense and regulate translation levels. *Nat Commun* **9:** 5074. doi:10.1038/s41467-018-07542-x.

Hegg LA, Kou M, Thurlow DL. 1990. Recognition of the tRNA-like structure in tobacco mosaic viral RNA by ATP/CTP:tRNA nucleotidyltransferases from *Escherichia coli* and *Saccharomyces*

cerevisiae. *J Biol Chem* **265:** 17441–17445. doi:10.1016/S0021-9258(18)38182-1

Hema M, Gopinath K, Kao C. 2005. Repair of the tRNA-like CCA sequence in a multipartite positive-strand RNA virus. *J Virol* **79:** 1417–1427. doi:10.1128/JVI.79.3.1417-1427.2005

Hogg JR. 2016. Viral evasion and manipulation of host RNA quality control pathways. *J Virol* **90:** 7010–7018. doi:10.1128/JVI.00607-16

Hou YM. 1997. Discriminating among the discriminator bases of tRNAs. *Chem Biol* **4:** 93–96. doi:10.1016/S1074-5521(97)90252-0

Hwang JN, Oh CS, Kang BC. 2013. Translation elongation factor 1B (eEF1B) is an essential host factor for Tobacco mosaic virus infection in plants. *Virology* **439:** 105–114. doi:10.1016/j.virol.2013.02.004

Ijberg B, Philipson L. 1972. Binding of histidine to tobacco mosaic virus RNA. *Biochem Biophys Res Commun* **48:** 927–932. doi:10.1016/0006-291X(72)90697-3

Jaafar ZA, Kieft JS. 2019. Viral RNA structure-based strategies to manipulate translation. *Nat Rev Microbiol* **17:** 110–123. doi:10.1038/s41579-018-0117-x

Jones RA, Steckelberg A-L, Vicens Q, Szucs MJ, Akiyama BM, Kieft JS. 2021. Different tertiary interactions create the same important 3-D features in a distinct flavivirus xrRNA. *RNA* **27:** 54–65. doi:10.1261/rna.077065.120

Joshi RL, Chapeville F, Haenni AL. 1985. Conformational requirements of tobacco mosaic virus RNA for aminoacylation and adenylation. *Nucleic Acids Res* **13:** 347–354. doi:10.1093/nar/13.2.347

Joshi RL, Ravel JM, Haenni AL. 1986. Interaction of turnip yellow mosaic virus Val-RNA with eukaryotic elongation factor EF-1α. Search for a function. *EMBO J* **5:** 1143–1148. doi:10.1002/j.1460-2075.1986.tb04339.x

Kalvari I, Argasinska J, Quinones-Olvera N, Nawrocki EP, Rivas E, Eddy SR, Bateman A, Finn RD, Petrov AI. 2018. Rfam 13.0: shifting to a genome-centric resource for non-coding RNA families. *Nucleic Acids Res* **46:** D335–D342. doi:10.1093/nar/gkx1038

Kim H, Cordero P, Das R, Yoon S. 2013. HiTRACE-Web: an online tool for robust analysis of high-throughput capillary electrophoresis. *Nucleic Acids Res* **41:** 492–498. doi:10.1093/nar/gkt501

King AMQ, Adams MJ, Carstens EB, Lefkowitz EJ. 2012. *Virus taxonomy: ninth report of the international committee on taxonomy of viruses*. Elsevier, NY.

Kladwang W, VanLang CC, Cordero P, Das R. 2011. A two-dimensional mutate-and-map strategy for non-coding RNA structure. *Nat Chem* **3:** 954–962. doi:10.1038/nchem.1176

Kladwang W, Mann TH, Becka A, Tian S, Kim H, Yoon S, Das R. 2014. Standardization of RNA chemical mapping experiments. *Biochemistry* **53:** 3063–3065. doi:10.1021/bi5003426

Kohl RJ, Hall TC. 1974. Aminoacylation of RNA from several viruses: amino acid specificity and differential activity of plant, yeast and bacterial synthetases. *J Gen Virol* **25:** 257–261. doi:10.1099/0022-1317-25-2-257

Lee S, Kim H, Tian S, Lee T, Yoon S, Das R. 2015. Automated band annotation for RNA structure probing experiments with numerous capillary electrophoresis profiles. *Bioinformatics* **31:** 2808–2815. doi:10.1093/bioinformatics/btv282

Levitt M. 1969. Detailed molecular model for transfer ribonucieic acid. *Nature* **224:** 759–763. doi:10.1038/224759a0

Li D, Wei T, Abbott CM, Harrich D. 2013. The unexpected roles of eukaryotic translation elongation factors in RNA virus replication and pathogenesis. *Microbiol Mol Biol Rev* **77:** 253–266. doi:10.1128/MMBR.00059-12

Litvak S, Tarrago-Litvak L, Chapeville F. 1973. Turnip yellow mosaic virus RNA as substrate of the transfer RNA nucleotidyltransferase. *J Virol* **11:** 238–242. doi:10.1128/JVI.11.2.238-242.1973

Lu X, Huang J, Wu S, Zheng Q, Liu P, Feng H, Su X, Fu H, Xi Q, Wang G. 2020. The tRNA-like small noncoding RNA mascRNA promotes global protein translation. *EMBO Rep* **21:** e49684. doi:10.15252/embr.201949684

Mans KMW, Pleij CWA, Bosch L. 1991. tRNA-like structures. structure, function and evolutionary significance. *Eur J Biochem* **201:** 303–324. doi:10.1111/j.1432-1033.1991.tb16288.x

Matsuda D, Dreher TW. 2004. The tRNA-like structure of Turnip yellow mosaic virus RNA is a 3′-translational enhancer. *Virology* **321:** 36–46. doi:10.1016/j.virol.2003.10.023

McCormack JC, Yuan X, Yingling YG, Kasprzak W, Zamora RE, Shapiro BA, Simon AE. 2008. Structural domains within the 3′ untranslated region of turnip crinkle virus. *J Virol* **82:** 8706–8720. doi:10.1128/JVI.00416-08

Nawrocki EP, Eddy SR. 2013. Infernal 1.1: 100-fold faster RNA homology searches. *Bioinformatics* **29:** 2933–2935. doi:10.1093/bioinformatics/btt509

Nissen P, Kjeldgaard M, Thirup S, Polekhina G, Reshetnikova L, Clark BFC, Nyborg J. 1995. Crystal structure of the ternary complex of Phe-tRNAPhe, EF-Tu, and a GTP analog. *Science* **270:** 1464–1472. doi:10.1126/science.270.5241.1464

Olsthoorn RCL, Haasnoot PCJ, Bol JF. 2004. Similarities and differences between the subgenomic and minus-strand promoters of an RNA plant virus. *J Virol* **78:** 4048–4053. doi:10.1128/JVI.78.8.4048-4053.2004

Osman TAM, Hemenway CL, Buck KW. 2000. Role of the 3′ tRNA-like structure in tobacco mosaic virus minus-strand RNA synthesis by the viral RNA-dependent RNA polymerase in vitro. *J Virol* **74:** 11671–11680. doi:10.1128/JVI.74.24.11671-11680.2000

Pathak KB, Pogany J, Nagy PD. 2011. Non-template functions of the viral RNA in plant RNA virus replication. *Curr Opin Virol* **1:** 332–338. doi:10.1016/j.coviro.2011.09.011

Perreault J, Weinberg Z, Roth A, Popescu O, Chartrand P, Ferbeyre G, Breaker RR. 2011. Identification of hammerhead ribozymes in all domains of life reveals novel structural variations. *PLoS Comput Biol* **7:** e1002031. doi:10.1371/journal.pcbi.1002031

Perret V, Florentz C, Dreher T, Giege R. 1989. Structural analogies between the 3′ tRNA-like structure of brome mosaic virus RNA and yeast tRNATyr revealed by protection studies with yeast tyrosyl-tRNA synthetase. *Eur J Biochem* **185:** 331–339. doi:10.1111/j.1432-1033.1989.tb15120.x

Pinck M, Yot P, Chapeville F, Duranton HM. 1970. Enzymatic binding of valine to the 3′ end of TYMV-RNA. *Nature* **226:** 954–956. doi:10.1038/226954a0

Pisareva VP, Pisarev AV, Fernández IS. 2018. Dual tRNA mimicry in the cricket paralysis virus IRES uncovers an unexpected similarity with the hepatitis C virus IRES. *Elife* **7:** e34062. doi:10.7554/eLife.34062

Rao ALN, Cheng Kao C. 2015. The brome mosaic virus 3′ untranslated sequence regulates RNA replication, recombination, and virion assembly. *Virus Res* **206:** 46–52. doi:10.1016/j.virusres.2015.02.007

Rietveld K, Linschooten K, Pleij CWA, Bosch L. 1984. The three-dimensional folding of the tRNA-like structure of tobacco mosaic virus RNA. A new building principle applied twice. *EMBO J* **3:** 2613–2619. doi:10.1002/j.1460-2075.1984.tb02182.x

Rivas E, Clements J, Eddy SR. 2016. A statistical test for conserved RNA structure shows lack of evidence for structure in lncRNAs. *Nat Methods* **14:** 45–48. doi:10.1038/nmeth.4066

Rivas E, Clements J, Eddy SR. 2020. Estimating the power of sequence covariation for detecting conserved RNA structure. *Bioinformatics* **36:** 3072–3076. doi:10.1093/bioinformatics/btaa080

Roth A, Breaker RR. 2009. The structural and functional diversity of metabolite-binding riboswitches. *Annu Rev Biochem* **78:** 305–334. doi:10.1146/annurev.biochem.78.070507.135656

Rould MA, Perona JJ, Söll D, Steitz TA. 1989. Structure of *E. coli* glutaminyl-tRNA synthetase complexed with RNA^{Gln} and ATP at 2.8 A resolution. *Science* **246:** 1135–1142. doi:10.1126/science.2479982

Rudinger J, Florentz C, Giegé R. 1994. Histidylation by yeast HisRS of tRNA or tRNA-like structure relies on residues-1 and 73 but is dependent on the RNA context. *Nucleic Acids Res* **22:** 5031–5037. doi:10.1093/nar/22.23.5031

Rudinger J, Felden B, Florentz C, Giegé R. 1997. Strategy for RNA recognition by yeast histidyl-tRNA synthetase. *Bioorganic Med Chem* **5:** 1001–1009. doi:10.1016/S0968-0896(97)00061-8

Rudinger-Thirion J, Olsthoorn RCL, Giegé R, Barends S. 2006. Idiosyncratic behaviour of tRNA-like structures in translation of plant viral RNA genomes. *J Mol Biol* **355:** 873–878. doi:10.1016/j.jmb.2005.11.023

Salomon R, Sela I, Soreq H, Giveon D, Littauer UZ. 1976. Enzymatic acylation of histidine to tobacco mosaic virus RNA. *Virology* **71:** 74–84. doi:10.1016/0042-6822(76)90095-7

Sherlock ME, Hartwick EW, Macfadden A, Kieft JS. 2021. Structural diversity and phylogenetic distribution of valyl tRNA-like structures in viruses. *RNA* **27:** 27–39. doi:10.1261/rna.076968.120

Simon AE, Miller WA. 2013. 3′ cap-independent translation enhancers of plant viruses. *Annu Rev Microbiol* **67:** 21–42. doi:10.1146/annurev-micro-092412-155609

Singh RN, Dreher TW. 1997. Turnip yellow mosaic virus RNA-dependent RNA polymerase: initiation of minus strand synthesis in vitro. *Virology* **233:** 430–439. doi:10.1006/viro.1997.8621

Steckelberg A-L, Akiyama BM, Costantino DA, Sit TL, Nix JC, Kieft JS. 2018. A folded viral noncoding RNA blocks host cell exoribonucleases through a conformationally dynamic RNA structure. *Proc Natl Acad Sci* **115:** 6404–6409. doi:10.1073/pnas.1802429115

Sun Y, Ma L. 2019. New insights into long non-coding RNA *MALAT1* in cancer and metastasis. *Cancers (Basel)* **11:** 1–12. doi:10.3390/cancers11020216

Tian Q, Wang C, Liu Y, Xie W. 2015. Structural basis for recognition of G-1-containing tRNA by histidyl-tRNA synthetase. *Nucleic Acids Res* **43:** 2980–2990. doi:10.1093/nar/gkv129

Tuplin A. 2015. Diverse roles and interactions of RNA structures during the replication of positive-stranded RNA viruses of humans and animals. *J Gen Virol* **96:** 1497–1503. doi:10.1099/vir.0.000066

Webb CHT, Riccitelli NJ, Ruminski DJ, Lupták A. 2009. Widespread occurrence of self-cleaving ribozymes. *Science* **326:** 953. doi:10.1126/science.1178084

Weinberg Z, Breaker RR. 2011. R2R - software to speed the depiction of aesthetic consensus RNA secondary structures. *BMC Bioinformatics* **12:** 3. doi:10.1186/1471-2105-12-3

Weis F, Bron P, Giudice E, Rolland JP, Thomas D, Felden B, Gillet R. 2010. tmRNA-SmpB: a journey to the centre of the bacterial ribosome. *EMBO J* **29:** 3810–3818. doi:10.1038/emboj.2010.252

Westhof E, Auffinger P. 2001. tRNA structure. *Encycl LIFE Sci* 1–11. doi: 10.1038/npg.els.0000527.

Williams KP, Bartel DP. 1995. Phylogenetic analysis of tmRNA secondary structure. *RNA* **2:** 1306–1310.

Wilusz JE, Freier SM, Spector DL. 2008. 3′ end processing of a long nuclear-retained non-coding RNA yields a tRNA-like cytoplasmic RNA. *Cell* **135:** 919–932. doi:10.1016/j.cell.2008.10.012

Xiong Y, Steitz TA. 2004. Mechanism of transfer RNA maturation by CCA-adding enzyme without using an oligonucleotide template. *Nature* **430:** 640–645. doi:10.1038/nature02711

Yamaji Y, Kobayashi T, Hamada K, Sakurai K, Yoshii A, Suzuki M, Namba S, Hibi T. 2006. In vivo interaction between Tobacco mosaic virus RNA-dependent RNA polymerase and host translation elongation factor 1A. *Virology* **347:** 100–108. doi:10.1016/j.virol.2005.11.031

Yoon S, Kim J, Hum J, Kim H, Park S, Kladwang W, Das R. 2011. HiTRACE: high-throughput robust analysis for capillary electrophoresis. *Bioinformatics* **27:** 1798–1805. doi:10.1093/bioinformatics/btr277

Zeenko V V, Ryabova LA, Spirin AS, Rothnie HM, Hess D, Browning KS, Hohn T. 2002. Eukaryotic elongation factor 1A interacts with the upstream pseudoknot domain in the 3′ untranslated region of tobacco mosaic virus RNA. *J Virol* **76:** 5678–5691. doi:10.1128/JVI.76.11.5678-5691.2002

An expanded class of histidine-accepting viral tRNA-like structures

Conner J. Langeberg, Madeline E. Sherlock, Andrea MacFadden, et al.

RNA 2021 27: 653-664 originally published online April 2, 2021
Access the most recent version at doi:10.1261/rna.078550.120